Korean J. Chem. Eng., 33(2), 490-499 (2016)
DOI: 10.1007/s11814-015-0183-y

pISSN: 0256-1115
eISSN: 1975-7220

CO_x-free hydrogen and carbon nanofibers production by methane decomposition over nickel-alumina catalysts

Nima Bayat*, Mehran Rezaei*,,†, and Fereshteh Meshkani***

*Catalyst and Advanced Materials Research Laboratory, Chemical Engineering Department, Faculty of Engineering, University of Kashan, Kashan, Iran
**Institute of Nanoscience and Nanotechnology, University of Kashan, Kashan, Iran
(*Received 28 March 2015 • accepted 28 August 2015*)

Abstract−Nickel catalysts supported on mesoporous nanocrystalline gamma alumina with various nickel loadings were prepared and employed for thermocatalytic decomposition of methane into CO_x-free hydrogen and carbon nanofibers. The prepared catalysts with different nickel contents exhibited mesoporous structure with high surface area in the range of 121.3 to 66.2 m^2g^{-1}. Increasing in nickel content decreased the pore volume and increased the crystallite size. The catalytic results revealed that the nickel content and operating temperature both play important roles on the catalytic performance of the prepared catalysts. The results showed that increasing in reaction temperature increased the initial conversion of catalysts and significantly decreased the catalyst lifetime. Scanning electron microscopy (SEM) analysis of the spent catalysts evaluated at different temperatures revealed the formation of intertwined carbon filaments. The results showed that increasing in reaction temperature decreased the diameters of nanofibers and increased the formation of encapsulating carbon.

Keywords: Methane Decomposition, Hydrogen, CO_x-free, Carbon Nanofibers, Nickel, Alumina

INTRODUCTION

Continuous growth in global population and economic development increase energy demand that is mainly supplied by combustion of fossil fuels, which releases large quantities of greenhouse gases, especially carbon dioxide. This procedure leads to serious environmental problems such as global warming and the acid rain. Concern over these environmental effects has created a major challenge to find clean energy resources [1-6].

Hydrogen is the most abundant and the simplest element in the world. It is known as a clean fuel and can be a promising alternative for fossil fuels, especially, with development of PEM fuel cells [7,8]. In addition, H_2 is used as a feedstock in different industrial applications such as oil refineries, ammonia and methanol production [9]. The amount of energy generated by hydrogen combustion is 2.4, 2.8 or 4 times higher than that of methane, gasoline or coal combustion, respectively [1]. Advantages of hydrogen as the most promising energy carriers have increased its demand. Therefore, many researchers have focused on the development of efficient, economic and environmentally friendly methods for hydrogen production [10].

Currently, steam reforming and partial oxidation of hydrocarbons and especially natural gas are the most important methods for commercial production of hydrogen [2,11-15]. However, in addition to high energy consumption these processes produce large amount of carbon oxides, which needs the complicated and expensive separation methods for H_2 purification [16,17].

Methane thermocatalytic decomposition is an attractive alternative way for clean hydrogen production because of low energy consumption and lack of carbon oxide production [18-20].

$$CH_4 \leftrightarrow C+2H_2 \qquad \Delta H^0_{298}=74.8\ kJ/mol \tag{1}$$

The energy requirement for H_2 production in this process is 37.8 kJ/mol H_2, which is significantly less than that 63.3 kJ/mol H_2 for methane steam reforming process [2]. In addition to CO_x-free hydrogen production, methane thermocatalytic decomposition generates carbon nanotubes and nanofibers. These valuable materials for their excellent surface property, high mechanical strength, high resistance to strong acids and bases, high electric conductivity and high surface area can be used in many applications such as adsorbent, catalyst and catalyst support, composite material and conductive polymers [21,22].

In general, Fe, Co and Ni have sufficient activity for methane thermocatalytic decomposition reaction. Nickel-based catalysts exhibit higher activity for methane cracking compared to the iron group metals [4,23]. In addition, cobalt has toxicity issues and higher cost compared to nickel. Comparison of the activity of these metals illustrates that the catalytic activity in methane cracking reaction for the iron group metals is: Ni>Co>Fe [4,24]. These metals have partially filled 3d orbitals, which facilitate the decomposition of the hydrocarbon molecules by partially accepting electrons [25].

The mechanism of the decomposition of methane and carbon fibers growth can be summarized as such that methane decomposes at the gas/metal interface, producing carbon which dissolves and diffuses through and around the catalyst particle to the metal/support interface, detaching the catalyst particle from the support,

†To whom correspondence should be addressed.
E-mail: rezaei@kashanu.ac.ir

forming a filament with the catalyst particle on the filament's tip [24,26-31].

The objective of the present work is the development of nickel-based catalysts supported on mesoporous nanocrystalline gamma alumina and its application in methane thermocatalytic decomposition reaction for the production of CO_x-free hydrogen and carbon nanofibers. In this article, Ni/Al_2O_3 catalysts with different nickel loadings were prepared by the wet impregnation method and catalytic tests were performed to investigate the effect of nickel loading and reaction temperature on the activity and stability of the prepared catalysts. In addition, the effect of calcination temperature was investigated on the textural and catalytic properties of the prepared catalysts.

EXPERIMENTAL

1. Sample Preparation

The catalyst support was prepared by the sol-gel method. For this purpose, aluminum tri-isopropylate ($C_9H_{21}AlO_3$, Merck) was first hydrolyzed in distillated water by stirring for 1 h at 80-85 °C. Subsequently, HNO_3 was added drop wise with HNO_3 to Al molar ratio of 1 : 1 and the prepared sol was refluxed for 12 h at 98 °C. After that, the sol was kept for 2 h at 98 °C in air atmosphere. After this step the sol became quite viscous. The resulting gel was then dried overnight at 80 °C and calcined at 450 °C for 4 h. The catalysts with different nickel contents were prepared by the wet impregnation method. For this purpose, the calcined catalyst support was impregnated with an aqueous solution of nickel nitrate ($Ni(NO_3)_2 \cdot 6H_2O$, Merck) with appropriate concentration to obtain desired content of nickel. After that the impregnated samples were dried at 80 °C for 10 h and calcined at different temperatures for 5 h.

2. Characterization

To examine the crystallinity of the prepared samples, powder X-ray diffraction (XRD) analysis was performed using an X-ray diffractometer (PANalyticalX'Pert-Pro) with a Cu-Kα monochromatized radiation source and a Ni filter in the range 2θ=10-80°. The N_2 adsorption/desorption analysis was at the boiling temperature of nitrogen (−196 °C) using an automated gas adsorption analyzer (Tristar 3020, Micromeritics). The samples were purged with nitrogen gas for 2 h at 200 °C using VacPrep 061 degas system (Micromeritics). Temperature programmed reduction (TPR) analysis was performed for evaluating the reduction properties of the prepared catalysts with a Micromeritics chemisorb 2750 gas-adsorption equipment. In the TPR measurement, 100 mg catalyst was subjected to a heat treatment (10 °C/min) in a gas flow (30 ml/min) containing a mixture of H_2 : Ar (10 : 90). Prior to TPR experiment, the samples were heat treated under an inert atmosphere (Ar) at 200 °C for 1 h. The H_2 uptake amount during the reduction was measured with a thermal conductivity detector (TCD). Temperature-programmed oxidation (TPO) of the spent catalysts involved using a similar apparatus as described for TPR analysis by introducing a gas flow (30 ml/min) containing a mixture of O_2 : He (5 : 95). In this analysis the temperature was increased up to 800 °C at a heating rate of 10 °C/min. Scanning electron microscopy (SEM) analysis was performed with a VEGA TESCAN electron microscope operated at 30 kV.

3. Catalytic Evaluation

The methane decomposition reaction was performed in a tubular fixed bed quartz micro-reactor under atmospheric pressure. For each test, 50 mg of the prepared sample was crushed and sieved to 35-70 mesh and charged into the reactor. An omega K-type thermocouple was used to measure the reaction temperature. Prior to reaction, the catalysts were reduced by a pure flow of H_2 with flow rate of 25 ml/min at 700 °C for 3 h. The feed gas contained 30 vol% CH_4 and 70 vol% N_2 and the flow rates were controlled by Bronkhorst High-Tech mass flow meter/controllers EL-FLOW® Select Series. The effluent gases from the reactor were analyzed by a gas chromatograph (Varian, model 3400) equipped with a TCD detector and a Carboxen 1000 column.

RESULTS AND DISCUSSION

1. Structural Properties

The structural properties of the catalyst support and calcined catalysts with different nickel contents are reported in Table 1. As can be seen, the catalyst support exhibits high specific surface area and pore volume. In addition, the catalyst support has a small crystallite size in nano scale. It is seen that increasing in Ni loading decreased the specific surface area and pore volume and increased the average crystallite size (Table 1). The reported crystallite sizes

Table 1. Structural properties of catalysts

Catalyst	BET surface area[a] ($m^2 \cdot g^{-1}$)	Particle size[b] D_{BET} (nm)	Pore volume[c] ($cm^3 \cdot gr^{-1}$)	Pore size[d] (nm)	Crystal size[e] D_{XRD} (nm)
Al_2O_3 (support)	188.2	8.06	0.65	8.05	7.63
30 wt% Ni/Al_2O_3	121.3	10.07	0.23	6.58	18.30
40 wt% Ni/Al_2O_3	105.6	10.92	0.22	6.59	20.75
50 wt% Ni/Al_2O_3	89.2	12.27	0.20	7.93	24.27
60 wt% Ni/Al_2O_3	66.1	15.81	0.13	7.20	26.62

[a]Calculated by the Brunauer-Emmett-Teller (BET) equation

[b]Calculated by $D=6000/\rho^*S_{BET}$

[c]Barrett-Joyner-Halenda (BJH) desorption pore volume

[d]Barrett-Joyner-Halenda (BJH) desorption average pore diameter

[e]Average NiO crystalline size determined using Scherrer equation

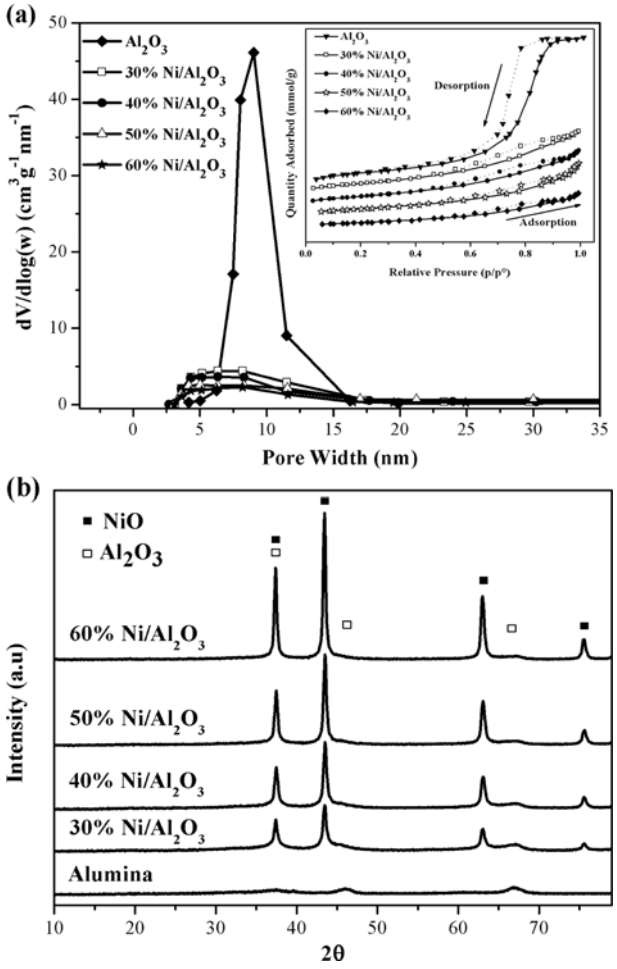

Fig. 1. (a) N_2 adsorption/desorption isotherms and pore size distributions, (b) XRD patterns of the alumina support and prepared samples calcined at 450 °C.

were calculated by the Debye-Scherrer equation for the diffraction peaks at 2θ=37.4°, 43.4°, 63.2° and 75.3°, corresponding to (111), (200), (220) and (311) planes of NiO, respectively. The decrease in surface area and pore volume may be caused by partial blockage of the alumina pores with nickel oxide clusters and/or a partial collapse of the mesoporous structure. In addition, the increase in the crystallite size of catalysts may be caused by particle agglomeration.

Fig. 1(a) shows the N_2 adsorption/desorption isotherms of catalyst support and calcined catalysts at 450 °C. According to IUPAC standard, the catalyst support exhibited the IV type isotherm with H2 hysteresis loop. The H2 shaped hysteresis loop revealed that the catalyst support has mesoporous structure with cylindrical-shaped channels with nonuniform pores [32,33]. As can be seen, the addition of nickel to catalyst support significantly affected the N_2 adsorption/desorption isotherm. The prepared catalysts exhibited V type isotherms with H3 hysteresis loops, which are the significant features for mesoporous materials.

This type of hysteresis is usually found in solids consisting of aggregates or agglomerates of particles forming slit shaped pores (plates or edged particles like cubes), with nonuniform size and/or shape [32].

As shown in Fig. 1(a), increasing in nickel content shifted the formation of hysteresis loops to higher partial pressure, which is the indication of a decline in the number of mesopores and the specific surface area. This is in agreement with the results reported in Table 1 [22,34].

Moreover, the pore size distributions of the prepared samples are shown in Fig. 1(a). It is seen that the pore size distributions of the prepared samples are in the range of 2.5-20 nm. The addition of nickel shifted the pore size distribution to smaller sizes, due to partial coverage of pores by nickel oxide. On the other hand, increasing in nickel loading blocks the pores and intensively declines the curve height.

XRD patterns of catalyst support and calcined catalysts with various nickel contents are shown in Fig. 1(b). In all catalysts, diffraction peaks at 2θ=37.4°, 43.4°, 63.2° and 75.3° belonged to NiO phase (JCPDS. 73-1519) and diffraction peaks at 2θ=37.4°, 46.1° and 66.9° assigned to alumina (JCPDS. 01-1308).

γ-Al_2O_3 has a pseudospinel structure and its lattice parameters are very close to that of nickel aluminate, so the identification of these phases is difficult due to peak overlapping. It is well known that Ni^{2+} preferentially incorporates into the tetrahedral vacancies of Al_2O_3 at low nickel loading, and the ratio of Ni^{2+} occupying the octahedral vacancies of gamma-Al_2O_3 increases with increase in nickel loading. Each peak shifts to lower temperature with increasing in nickel loading, which greatly leads to a diminishing in metal-support interaction [35,36]. NiO particles in catalysts with high NiO contents tend to aggregate just as bulk NiO due to the weak interaction with alumina. The XRD results clearly showed that increasing in nickel loading increased the intensity of peaks related to NiO phase, an indication of increase in NiO crystallite size (Table 1). As can be seen, the catalyst with the highest nickel content exhibited the biggest NiO crystallite size as reported in Table 1.

Fig. 2 shows the XRD pattern of the reduced catalyst with 50 wt% nickel. In the XRD pattern, the diffraction peaks of Ni species observed at 2θ=44.7°, 52.1° and 76.5° were related to (111), (200) and (220) planes. The average nickel crystallite size in this

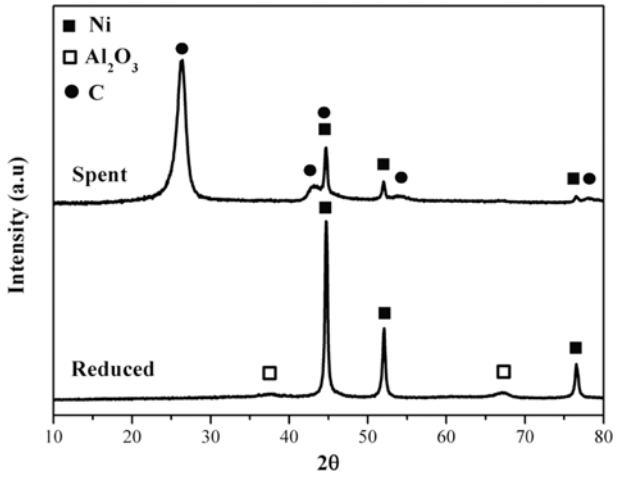

Fig. 2. XRD pattern of the reduced catalyst at 700 °C and spent catalyst with 50 wt% Ni (reaction conditions: CH_4 : N_2=3 : 7, GHSV=12,000 (ml·h^{-1}g$_{cat}^{-1}$). T=600 °C).

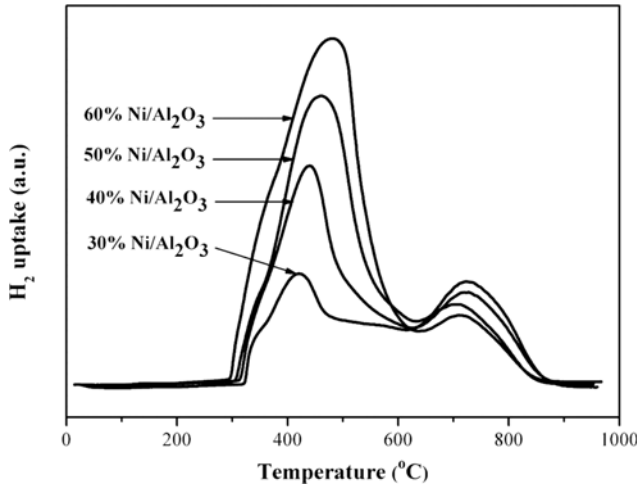

Fig. 3. TPR profiles of Ni/Al_2O_3 catalysts calcined at 450 °C.

catalyst was 26.36 nm. In addition, the diffraction peaks at 2θ= 37.5° and 67.1° were assigned to alumina (JCPDS. 01-1308). XRD analysis showed that the NiO phase was converted to Ni during the reduction process with hydrogen. Nickel is an active phase for the methane decomposition reaction.

2. Temperature Programmed Reduction Analysis (TPR)

The TPR analysis was performed to investigate the reduction behavior of the calcined catalysts. In conjunction with XRD analysis, it is also useful in determining the type of species present in the calcined catalysts. The TPR profiles of the Ni catalysts with different nickel content are shown in Fig. 3. Increasing in Ni loading increased the amount of H_2 uptake due to higher concentration of NiO in the catalyst. For all catalysts the shoulder peak at temperatures below 400 °C is attributed to reduction of agglomerated nickel oxides with weak interaction with Al_2O_3. The reduction peak in the temperature range between 400-600 °C is related to reduction of NiO species with stronger interaction with catalyst support. The reduction peak at temperature higher than 650 °C is assigned to the reduction of $NiAl_2O_4$. The increase in nickel content increased both the degree of agglomeration and size of nickel oxide particles, which caused a decrease in metal-support interaction. The decrease in metal-support interaction makes the reduction of NiO easier [35,37].

3. SEM Analysis

Fig. 4(a) shows the SEM images of the prepared alumina. These images confirm that the catalyst support has a nanostructure. SEM image of fresh 50 wt% Ni/Al_2O_3 catalyst is also shown in Fig. 4(b). The porosity decreased due to incorporation of nickel oxide into the catalyst support.

4. Catalytic Performance

Thermocatalytic decomposition of methane was performed to investigate the effects of operating temperature and nickel loading on the catalytic performance of the prepared catalysts. Fig. 5(a) shows the methane conversion of nickel catalysts with different nickel contents at various temperatures. The methane conversion increased with increasing temperature due to endothermic nature of the reaction. It is observed that increase in reaction temperature up to 650 °C improved the methane conversion, except for the catalyst with 60 wt% Ni. However, a further increase in reaction temperature beyond this value results into a decrease in methane conversion. The formation of encapsulating carbon and consequently the coverage of active sites is the main reason for intensive decline in methane conversion. This type of carbon is generated because of the imbalance between the rate of carbon production and transmission through the active sites [19].

As can be seen, increase in nickel loading up to 50 wt% increased the methane conversion, and further increase in nickel content caused a decrease in methane conversion. Higher nickel content and specific surface area increase the active site concentration and the dispersion, respectively. However, nickel dispersion decreases with increasing nickel content.

Thus, a clear understanding of these intricate relationships is nec-

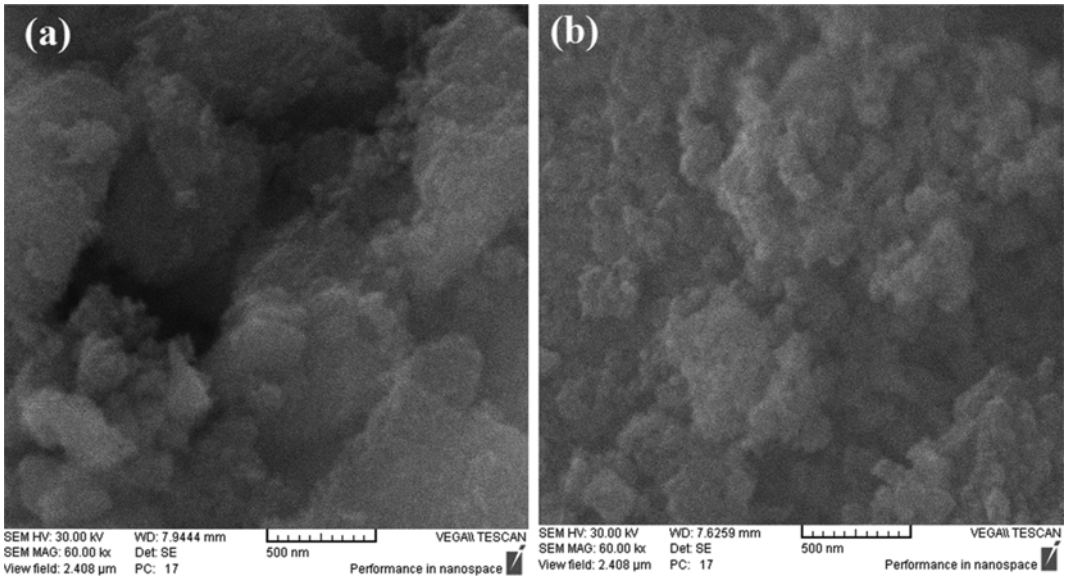

Fig. 4. SEM images of (a) prepared alumina with sol-gel method as catalyst support and (b) 50 wt% Ni/Al_2O_3 calcined at 450 °C.

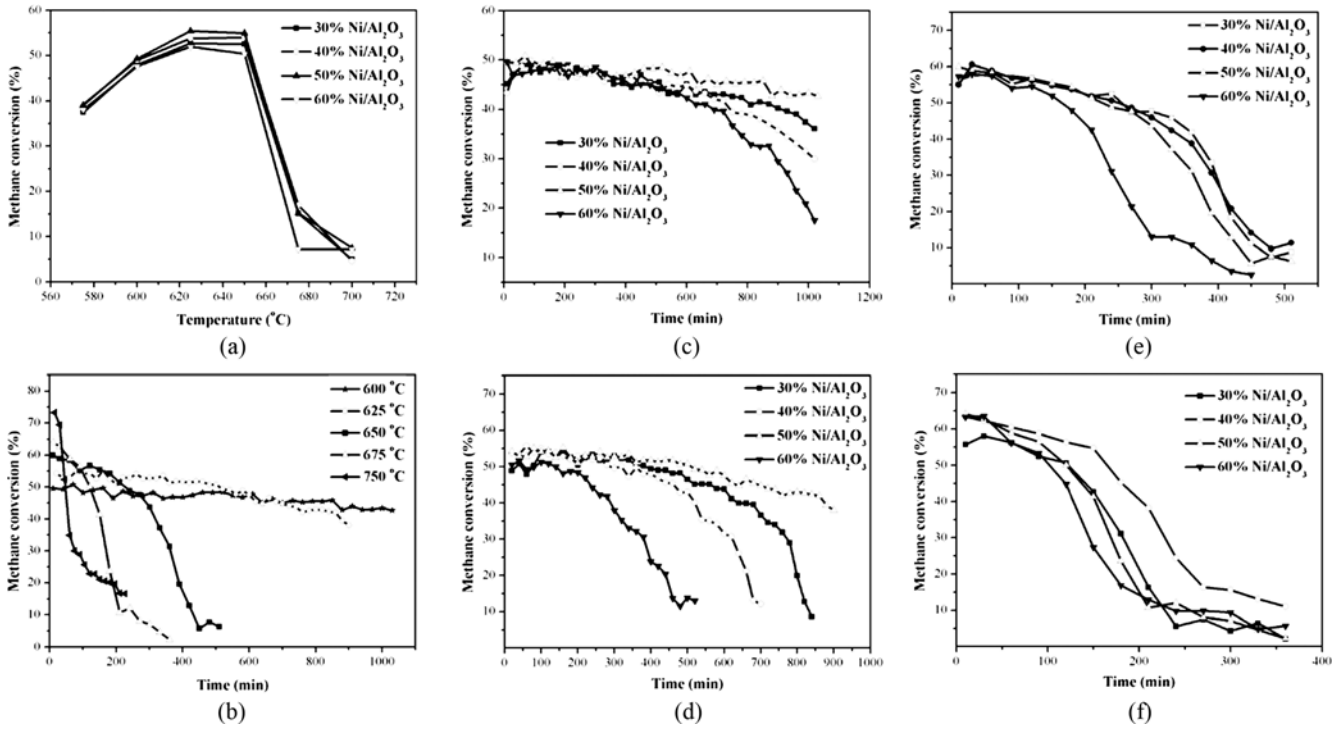

Fig. 5. (a) Effect of reaction temperature and Ni loading on methane conversion ($CH_4:N_2=3:7$, GHSV=24,000 ml·h^{-1}g$_{cat}^{-1}$), (b) stability of the 50 wt% Ni/Al_2O_3 catalyst at different temperatures ($CH_4:N_2=3:7$, GHSV=12,000 ml·h^{-1}g$_{cat}^{-1}$) and Stability of the Ni/Al_2O_3 catalysts with different nickel contents ($CH_4:N_2=3:7$, GHSV=12,000 ml·h^{-1}g$_{cat}^{-1}$) at (c) T=600 °C, (d) T=625 °C (e) T=650 °C, (f) T=675 °C.

essary to optimize activity and stability of the catalyst. As shown in Fig. 5(a), the highest methane conversion was observed for the catalyst with 50 wt% Ni.

Ermakova et al. [38] reported that at temperatures lower than 550 °C, the surface carbon concentration is low and does not achieve the degree of super saturation required for the nucleation of carbon filaments. Therefore, more carbon is deposited as encapsulating carbon, which causes catalyst deactivation. On the other hand, at high temperatures, the formation rate of surface carbon is high compared to the diffusion of carbon through the particle to form filaments. Because of this, the carbon accumulates on the catalyst surface and leads to a more rapid deactivation of the catalyst. Therefore, appropriate operating temperature can be in the range of 550-650 °C.

In the methane thermocatalytic decomposition process, the product quantity strongly depends on the catalyst stability. Hence, catalyst stability has an important role in process economics. Stability tests for all samples were therefore performed at different temperatures for better understanding of reaction behavior.

More nickel content increases the available active metal for reaction and it is useful to improve the catalyst stability. On the other hand, the interaction between metal and support becomes weak with increase in nickel loading, which leads to easier separation of the nickel particles from the support. As a result, tip growth mechanism for the formation of carbon nanofibers becomes dominant against base growth and catalyst life increases. But as mentioned, specific surface area decreases with increasing in nickel loading. The mentioned reasons reveal the importance of the optimized loading and operating temperature [22,34].

The results of stability tests at different temperatures are presented in Fig. 5(b)-(f). The catalytic stability at 600 °C is shown in Fig. 5(c). As can be seen, the catalyst with 50 wt% Ni exhibited higher stability compared to other catalysts during 1,000 min time on stream. The catalyst with 60 wt% Ni exhibited the lowest activity among the prepared catalysts. Specific surface area, dispersion and crystal size as structural properties of catalyst and reaction temperature as the most important operating condition in thermocatalytic decomposition of methane are effective factors on the catalytic performance. These parameters have opposite behaviors. For example, increasing in both surface area and nickel content is useful for catalytic performance, but increasing in nickel content decreases the surface area. Also, increasing in reaction temperature enhances the initial methane conversion and decreases the catalyst stability [7]. The 50 wt% Ni/Al_2O_3 catalyst created balance for these parameters, which led to the highest catalytic performance among the investigated samples at 600 °C.

The same trend was also observed for the catalysts evaluated at 625 °C (Fig. 5(d)). However, as can be seen, the deactivation rate is higher than that observed at 600 °C. The stability test showed that the catalysts at 650 °C and 675 °C exhibited a high degree of deactivation, which could be due to agglomeration of particles at high temperatures. On the other hand, a quasi-liquid state is created for nickel particles at high temperature. In this state metal particles are fragmented and encapsulated within the carbon fibers [2,39]. This phenomenon is one of the deactivation reasons that occurs usually at high temperatures and when the metal particles are in quasi-

liquid state [38,40]. As can be seen, the deactivation rate is more serious for the catalyst with the highest nickel loading.

Increasing in reaction temperature improved the initial conversion of methane and decreased the stability of catalyst. It is known that any factor that increases the rate of methane conversion without proportional increase in immigration rate of carbon leads to enhance of deactivation rate [7,19].

Because of the significant effect of operating temperature on the catalyst lifetime the stability test was performed over the 50%Ni/Al_2O_3 at different temperatures and the obtained results are shown in Fig. 5(b). As mentioned earlier, due to the endothermic nature of the reaction, increasing in reaction temperature increases the initial activity. It leads to increasing in rate of carbon production and breaks the balance between production and migration of carbon via active metals, which causes the accumulation and coverage of carbon on the metal surface. Formation of encapsulating carbon significantly decreases the catalyst lifetime, and increasing in reaction temperature also leads to generation of quasi-liquid and fragmented nickel particles, which are encapsulated within the carbon fibers [38,40,41].

5. Carbon Production

In the thermocatalytic decomposition of methane, besides the hydrogen, carbon nanofibers were also produced. Carbon growth involves a gas phase reaction on the surface which eventually dissolves in the metal and precipitates at a dislocation of the particle to form graphite [24,26-31].

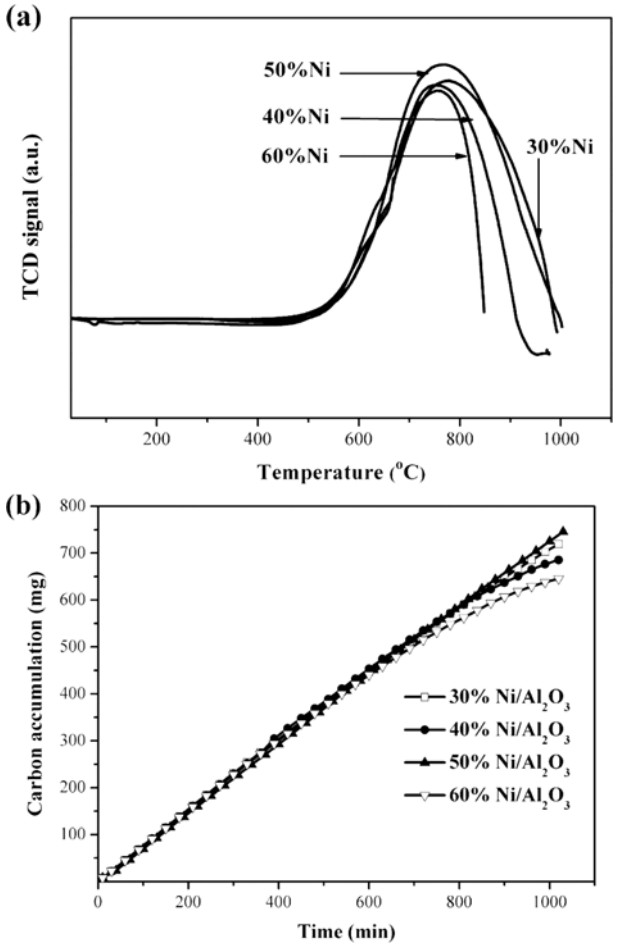

Fig. 6. TPO and carbon production profiles of the spent catalysts. Reaction conditions: $CH_4:N_2=3:7$, GHSV=12,000 ($ml \cdot h^{-1} g_{cat}^{-1}$), T=600 °C.

5-1. Characterization of the Spent Catalysts

Fig. 2 shows the XRD pattern of the spent 50 wt%Ni/Al_2O_3 catalyst after 1,000 min of reaction at 600 °C. The diffraction patterns at 2θ=44.5°, 52° and 76.5° are related to (111), (200) and (220) planes of cubic metallic nickel [JCPDS No. 01-087-0712] with an average crystallite size of 25.26 nm. The reflections at 2θ=26.5°, 42.9°, 44.6°, 54.5° and 78° are assigned to graphitic carbon [JCPSD No. 01-0640]. However, the peak located at 42.9° is indicative of the formation of quasi-amorphous nanocarbons [29]. The appearance of a graphitic carbon phase is dominant over metallic Ni phase.

The TPO profiles of the spent Ni/Al_2O_3 catalysts with different nickel content are shown in Fig. 6(a). Two peaks were observed in TPO profile of the spent catalysts. The first low temperature peak can be attributed to encapsulating carbon. This carbon can cover the active sites and lead to deactivation of catalyst. The high temperature peak was related to carbon nanofibers with crystalline structure. In addition, the amount of deposited carbon was calculated by carbon balance, and the carbon accumulation curves are depicted in Fig. 6(b). The results show that the 50%Ni/Al_2O_3 catalyst produced the highest amount of carbon, which is in agreement with TPO analysis.

The produced carbons were collected at the end of the reaction and investigated by SEM analysis. Fig. 7(a)-(c) show the morphology of the produced carbon in the catalytic decomposition of methane over 50 wt%Ni/Al_2O_3 catalyst at different temperatures. SEM analyses confirmed the formation of filamentous type carbon.

These filaments have a few nanometers diameter, while their length varies in micrometer scale. Because of the interwoven nature of them, it was not possible to investigate the correct length of these nanofibers.

In addition, the SEM images depict that the fiber diameters are close to the size of metallic nickel particles. This indicates that a Ni metal particle produces carbon nanofiber at the same size as itself. Bright points on the top of carbon filaments are related to metallic nickel particles that indicate tip growth mechanism was dominant for formation of carbon filaments.

Comparing these SEM images of the carbon filaments produced at different temperatures illustrates the effects of operating temperature on the morphology of carbon filaments. Reaction temperature has a significant effect on the morphology of carbon nanofibers. It is known that the perfect (solid) CNFs forms at the lower temperature and the higher temperature leads to produce of carbon nanotubes (CNTs) [42-44]. As can be seen in Fig. 7(a)-(c), with increasing in reaction temperature the diameter of filament decreases, which is due to creation of quasi-liquid state of metal particles and fragmentation of the metal particles [2].

However, with increasing temperature the number of bright spots was reduced, due to the carbon coverage of nickel surface on the tope of filament, which leads to inaccessibility of nickel as active metal and decline of methane conversion. This conclusion is in good agreement with the results obtained from Fig. 5, which show higher rate of deactivation at higher reaction temperatures.

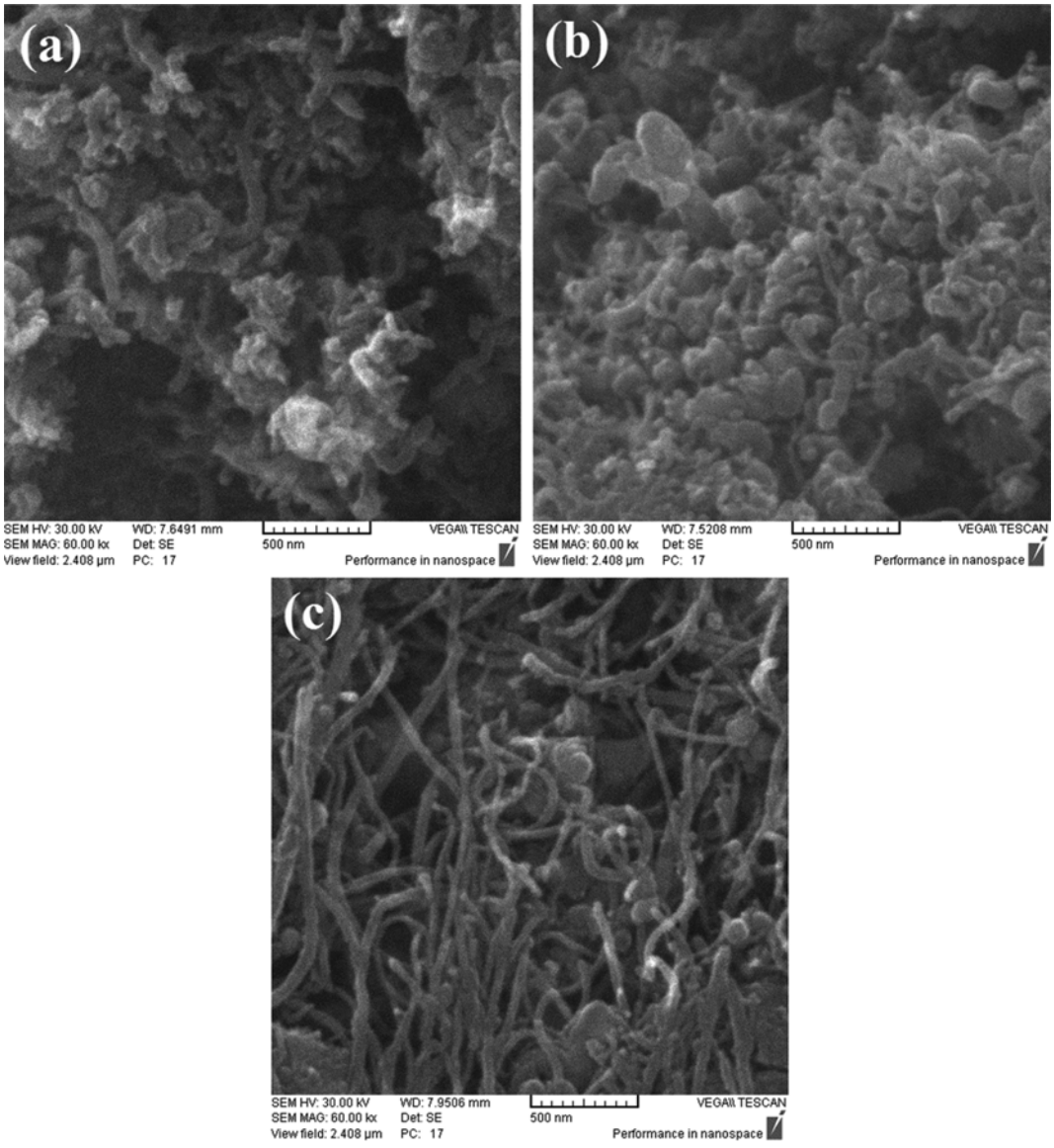

Fig. 7. SEM images of the spent 50 wt% Ni/Al_2O_3 catalyst (a) time on the stream=1020 min at 600 °C, (b) time on the stream=360 min at 675 °C and (c) time on the stream=225 min at 750 °C ($CH_4 : N_2$=3 : 7, GHSV=12,000 ml·$h^{-1}g_{cat}^{-1}$).

Table 2. Structural properties of 50 wt% Ni/Al_2O_3 calcined at different temperatures

Calcination temperature (°C)	BET surface[a] area (m^2g^{-1})	Particle size[b] D_{BET} (nm)	Pore volume[c] (cm^3g^{-1})	Pore size[d] (nm)	Crystal size[e] D_{XRD} (nm)
450	89.28	12.27	0.20	7.93	24.27
550	76.98	14.24	0.19	8.33	24.60
650	63.67	17.21	0.17	8.92	26.52

[a]Calculated by the BET equation
[b]Calculated by $D=6000/\rho^*S_{BET}$
[c]BJH desorption pore volume
[d]BJH desorption average pore diameter
[e]Average NiO crystalline size determined using Scherrer equation

6. Effect of Calcination Temperature

The structural properties of the catalysts calcined at different temperatures are presented in Table 2. The results revealed that the specific surface area decreased with increasing calcination temperature and consequently led to an increase in particle and pore sizes. The decrease in surface area is due to destruction of the mesoporous

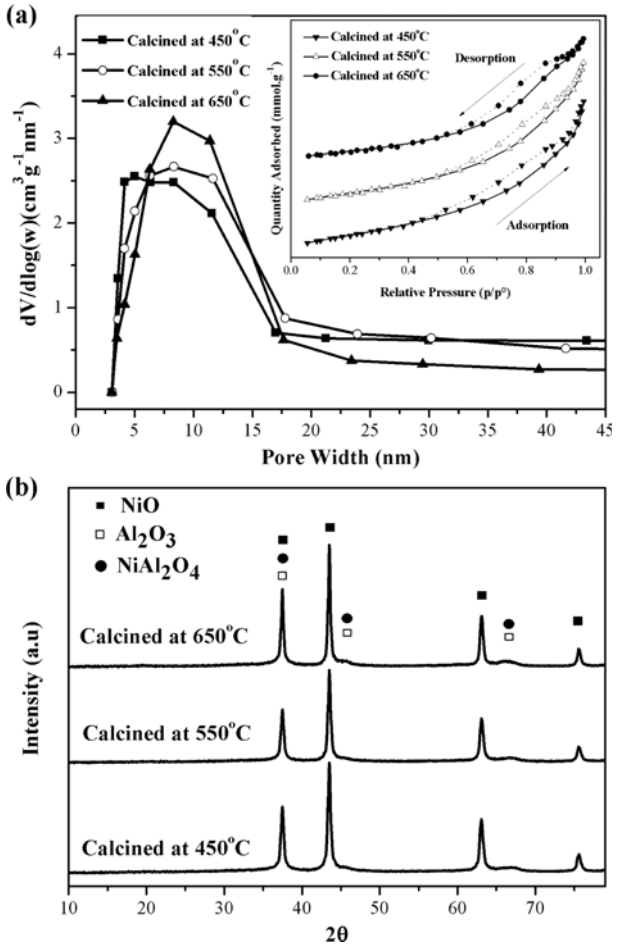

Fig. 8. (a) N_2 adsorption/desorption isotherms and pore size distributions, (b) XRD patterns of 50 wt% Ni/Al_2O_3 calcined at different temperatures.

structure at high temperatures. In addition, the NiO crystallite sizes were also increased with increasing in calcination temperature due to sintering of NiO crystals at high temperatures.

The N_2 adsorption/desorption isotherms and pore size distributions of the catalysts calcined at different temperatures are shown in Fig. 8(a). According to IUPAC standard, the isotherms are considered as V type with H3 hysteresis loop, which are the significant features for mesoporous materials. As shown in Fig. 8(a), increasing in calcination temperature shifted the formation of hysteresis loop to higher P/P_0 relative pressures, indicating the existence of larger pores for the samples calcined at higher temperatures. This leads to decrease in specific surface area, Table 2.

The pore size distributions of the calcined catalysts at different temperatures are shown in Fig. 8(a). The catalysts exhibited mesoporous structure in the range of 3-40 nm. Increasing in calcination temperature shifted the pore size distribution slightly to larger sizes.

Fig. 8(b) shows the XRD patterns of the 50 wt% Ni/Al_2O_3 catalyst calcined at different temperatures. Increase in calcination temperature leads to creation and increase the amount of $NiAl_2O_4$ phase in calcined catalysts, which is an inactive phase for reaction. The highest fraction of $NiAl_2O_4$ was observed on the catalyst calcined at 650 °C. Increasing in calcination temperature increased the intensities of XRD pattern, which is related to bigger crystallite size.

Moreover, as shown in Table 2, the average NiO crystallite size gradually increases from 24.7 to 26.5 nm with the increase in calcination temperature up to 650 °C. From Fig. 8(b), and Table 2, it can be concluded that crystal structure of the catalysts is affected by calcination temperature.

The TPR profiles of the 50 wt% Ni/Al_2O_3 catalysts calcined at different temperatures are shown in Fig. 8.

For calcined catalyst at 450 °C, the shoulder peak at 350 °C was attributed to reduction of agglomerated and bulk nickel oxide particles with weak interaction with Al_2O_3, and the reduction peak at 420 °C was related to reduction of NiO with stronger interaction with support. The reduction peak observed at 700 °C is related to $NiAl_2O_4$ reduction [37,45].

In Fig. 9, the interaction between NiO and support increased with increasing in calcination temperature. Therefore, the T_{max} of reduction peaks was shifted toward higher temperature. Also, in-

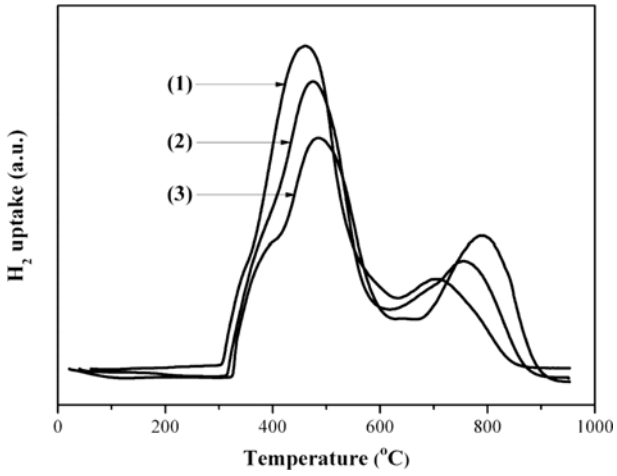

Fig. 9. TPR profiles of 50 wt% Ni/Al_2O_3 calcined at different temperatures.

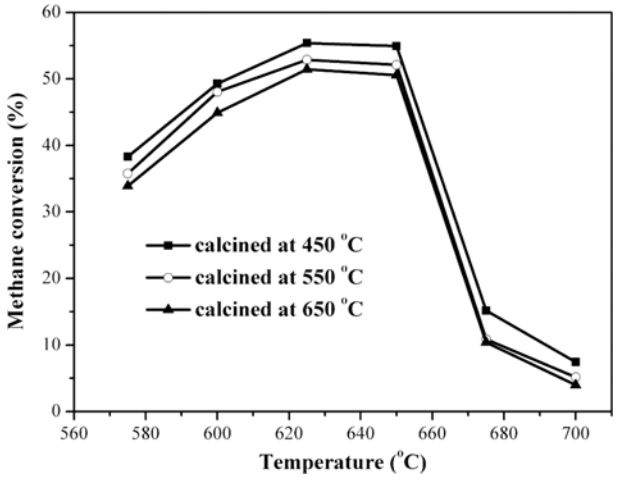

Fig. 10. Effect of calcination temperature on methane conversion of 50 wt%Ni/Al_2O_3 catalyst, Reaction conditions: $CH_4 : N_2 = 3 : 7$, GHSV=24,000 $ml \cdot h^{-1} g_{cat}^{-1}$.

creasing in calcination temperature decreased the peak area of low temperature peak and increased the peak area of high temperature peak, indicating the higher content of $NiAl_2O_4$ in catalyst calcined at higher temperatures.

Fig. 10 shows the methane conversion of the 50 wt% Ni/Al_2O_3 catalysts calcined at different temperatures. The increase in reaction temperature up to 625 °C improved the methane conversion, but further increase decreased the methane conversion.

In addition, in Fig. 10, increasing in calcination temperature decreased the methane conversion. Increasing in calcination temperature decreased the surface area as reported in Table 2. Increasing in calcination temperature increased the agglomeration of particles, growth of crystals and $NiAl_2O_4$ formation. All the mentioned properties have a negative effect on the catalytic activity [7,46-48].

CONCLUSIONS

Nickel catalysts supported on mesoporous nanocrystalline gamma alumina were employed as catalyst for catalytic decomposition of methane for production of CO_x-free hydrogen and carbon nanofibers. The results showed that the Ni/Al_2O_3 catalysts were highly active and stable in methane decomposition reaction. The catalysts' activity and stability were found to be strongly dependent on the nickel content and operating temperature.

The results revealed that the 50 wt% Ni/Al_2O_3 catalyst demonstrated higher activity and stability compared to other Ni catalysts at 625 °C and 650 °C. Higher reaction temperatures led to higher reaction rates and faster deactivation of the catalysts. Also, the methane conversion decreased in low reaction temperature. SEM analysis confirmed that the produced carbon was in filamentous form. Also, this analysis showed that the diameter of fibers was close to the size of metallic nickel particles. Comparing SEM images related to carbon filaments, which were produced at different temperatures, illustrates the effect of operating temperature on morphology of carbon filaments. Increasing in reaction temperature decreased the diameter of filaments.

ACKNOWLEDGEMENTS

The authors are grateful to University of Kashan for supporting this work by Grant No. 158426/50.

REFERENCES

1. H. F. Abbas and W. W. Daud, *Int. J. Hydrogen Energy*, **35**, 1160 (2010).
2. Y. Li, D. Li and G. Wang, *Catal. Today*, **162**, 1 (2011).
3. D. J. Wuebbles and A. K. Jain, *Fuel Processing Technol.*, **71**, 99 (2001).
4. A. M. Amin, E. Croiset and W. Epling, *Int. J. Hydrogen Energy*, **36**, 2904 (2011).
5. H. T. Jang, and W. S. Cha, *Korean J. Chem. Eng.*, **24**, 374 (2007).
6. J. U. Jung, W. Nam, K. J. Yoon and G. Y. Han, *Korean J. Chem. Eng.*, **24**, 674 (2007).
7. A. M. Amin, E. Croiset, C. Constantinou and W. Epling, *Int. J. Hydrogen Energy*, **37**, 9038 (2012).
8. H. Arandiyan, J. Li, L. Ma, S. Hashemnejad, M. Mirzaei, J. Chen, H. Chang, C. Liu, C. Wang and L. Chen, *J. Ind. Eng. Chem.*, **18**, 2103 (2012).
9. G. Marbán and T. Valdés-Solís, *Int. J. Hydrogen Energy*, **32**, 1625 (2007).
10. A. C. Lua and H. Y. Wang, *Appl. Catal. B: Environ.*, **132-133**, 469 (2013).
11. R. Kothari, D. Buddhi and R. Sawhney, *Renew. Sustain. Energy Rev.*, **12**, 553 (2008).
12. J. D. Holladay, J. Hu, D. L. King and Y. Wang, *Catal. Today*, **139**, 244 (2009).
13. A. Khalesi, H, Arandiyan and M. Parvari, *Chinese J. Catal.*, **29**, 960 (2008).
14. H. Arandiyan, Y. Peng, C. Liu, H. Chang and J. Li, *J. Chem. Technol. Biotechnol.*, **89**, 372 (2014).
15. M. H. Kim, E. K. Lee, J. H. Jun, G. Y. Han, S. J. Kong, B. K. Lee, T.-J. Lee and K. J. Yoon, *Korean J. Chem. Eng.*, **20**, 835 (2003).
16. R. Navarro, M. Pena and J. Fierro, *Chem. Reviews*, **107**, 3952 (2007).
17. J. T. Overpeck and J. E. Cole, *Annu. Rev. Environ. Resour.*, **31**, 1 (2006).
18. Q. Weizhong, L. Tang, W. Zhanwen, W. Fei, L. Zhifei, Guohua and L. Yongdan, *Appl. Catal. A: Gen.*, **260**, 223 (2004).
19. J. Chen, Y. Li, Z. Li and X. Zhang, *Appl. Catal. A: Gen.*, **269**, 179 (2004).
20. S. C. Lee, H. J. Seo and G. Y. Han, *Korean J. Chem. Eng.*, **30**, 1716 (2013).
21. M.-F. Yu, B. S. Files, S. Arepalli and R. S. Ruoff, *Phys. Review Lett.*, **84**, 5552 (2000).
22. S. K. Saraswat and K. K. Pant, *J. Natural Gas Sci. Eng.*, **13**, 52 (2013).
23. M. Ermakova and D. Y. Ermakov, *Catal. Today*, **77**, 225 (2002).
24. Y. Li, B. Zhang, X. Tang, Y. Xu and W. Shen, *Catal. Commun.*, **7**, 380 (2006).
25. A.-C. Dupuis, *Progress in Materials Science*, **50**, 929 (2005).
26. S. Helveg, C. Lopez-Cartes, J. Sehested, P. L. Hansen, B. S. Clausen, J. R. Rostrup-Nielsen, F. Abild-Pedersen and J. K. Nørskov, *Nature*, **427**, 426 (2004).
27. F. Abild-Pedersen, J. K. Nørskov, J. R. Rostrup-Nielsen, J. Sehested and S. Helveg, *Phys. Review B*, **73**, 115419 (2006).
28. W. Wang, H. Wang, Y. Yang and S. Jiang, *Int. J. Hydrogen Energy*, **37**, 9058 (2012).
29. J. C. Guevara, J. A. Wang, L. F. Chen, M. A. Valenzuela, P. Salas, A. García-Ruiz, J. A. Toledo, M. A. Cortes-Jácome, C. Angeles-Chavez and O. Novaro, *Int. J. Hydrogen Energy*, **35**, 3509 (2010).
30. J. Ashok, G. Raju, P. S. Reddy, M. Subrahmanyam and A. Venugopal, *Int. J. Hydrogen Energy*, **33**, 4809 (2008).
31. J. Ashok, M. Subrahmanyam and A. Venugopal, *Int. J. Hydrogen Energy*, **33**, 2704 (2008).
32. G. Leofanti, M. Padovan, G. Tozzola and B. Venturelli, *Catal. Today*, **41**, 207 (1998).
33. Z. Alipour, M. Rezaei and F. Meshkani, *Fuel*, **129**, 197 (2014).
34. A. E. Awadallah, A. A. Aboul-Enein and A. K. Aboul-Gheit, *Renewable Energy*, **57**, 671 (2013).
35. R. Wang, Y. Li, R. Shi and M. Yang, *J. Mol. Catal. A: Chemical*, **344**, 122 (2011).
36. M. Wu and D. M. Hercules, *J. Phys. Chem.*, **83**, 2003 (1979).
37. C. Li and Y. W. Chen, *Thermochim. Acta*, **256**, 457 (1995).
38. M. Ermakova, D. Y. Ermakov and G. Kuvshinov, *Appl. Catal. A:*

Gen., **201**, 61 (2000).
39. S. G. Zavarukhin and G. G. Kuvshinov, *Appl. Catal. A: Gen.*, **272**, 219 (2004).
40. Y. Li, J. Chen, Y. Ma, J. Zhao, Y. Qin and L. Chang, *Chem. Commun.*, **12**, 1141 (1999).
41. R. Baker, M. Barber, P. Harris, F. Feates and R. Waite, *J. Catal.*, **26**, 51 (1972).
42. J. L. Chen, X. M. Li, Y. D. Li and Y. N. Qin, *Chem. Lett.*, **32**, 424 (2003).
43. J. W. Snoeck, G. F. Froment, M. Fowles, *J. Catal.*, **169**, 240 (1997).
44. S. Takenaka, M. Ishida, M. Serizawa, E. Tanabe and K. Otsuka, *J. Phys. Chem. B*, **108**, 11464 (2004).
45. M. R. Quddus, M. M. Hossain and H. I. de Lasa, *Catal. Today*, **210**, 124 (2013).
46. Y. Echegoyen, I. Suelves, M. J. Lázaro, R. Moliner and J. M. Palacios, *J. Power Sources*, **169**, 150 (2007).
47. I. Suelves, M. Lázaro, R. Moliner, B. Corbella and J. Palacios, *Int. J. Hydrogen Energy*, **30**, 1555 (2005).
48. Y. Li, B. Zhang, X. Xie, J. Liu, Y. Xu and W. Shen, *J. Catal.*, **238**, 412 (2006).